10.202 A SIMULATION STUDY OF THE IMPACT OF SURFACE CLUTTERS ON SPACEBORNE PRECIPITATION RADAR SENSOR

Ramesh Nepal[1], Zhengzheng Li[1], Yan Zhang[1] and Lihua Li[2]
[1]Advanced Radar Research Center
University of Oklahoma
Norman, OK 73072
[2]NASA Goddard Space Flight Center

1. ABSTRACT

Surface clutter echoes through antenna and range sidelobes from pulse compression can severely interfere with the atmospheric radar returns near the earth surface. A radar simulator is developed to study the impacts of clutter interference from different types of earth surface. Simplified antenna pattern and pulse compression filter response models are used to investigate the worst case scenarios with reduced computation requirements. It is found that antenna sidelobe is the dominant source of surface clutter interference when the pulse compression range sidelobe is higher than -60 dB, while the distribution of clutter-contaminated radar resolution volumes depends on multiple factors including sensor and environment.

Keywords-spaceborne precipitation radar; radar simulator; surface clutter; antenna sidelobes; pulse compression

2. INTRODUCTION

Spaceborne atmospheric radars have been the key source of knowledge of the earth's climate and global water resource (Levizzani (2007)). One of the challenges in the designing phase of such radar systems is to predict its performance under various conditions. The complexity of the problem originates from factors such as thermal noise, finite receiver bandwidth, nonlinearities of the system and the interference/clutter from earth's surface through antenna and pulse compression sidelobes. To address these challenges, accurate sensor simulation plays an essential role (Pavone (2000)).

Impacts of ground-clutters on TRMM/GPM spaceborne radars have been extensively studied (Durden (2001), Hanado and Ihara (1992), and Tagawa (2007)). However, as the trend of future airborne and spaceborne generation precipitation radar (such as HIWRAP (Lihua (2008)) is employing full solid-state transceivers and pulse compression techniques, sidelobe interference from pulse compression and nonlinearities of the sensor system is becoming very important, which has not been fully investigated. The *combined* effect of antenna and range sidelobe has not been seriously studied in previous literature.

*Corresponding Author: Zhengzheng Li, School of Electrical and Computer Engineering, Advanced Radar Research Center, University of Oklahoma, Norman, OK 73072, Email: zhengzheng.li@ou.edu

This study incorporates the pulse compression receiver modeling into the existing radar clutter models, and provides a tool to predict the performance of future advanced spaceborne radar systems in term of sensing the near-surface weather phenomena. The radar parameters are mainly based on existing TRMM, but waveform parameters used in the HIWRAP system is also incorporated.

3. MODELS AND GEOMETRIES

3.1 Spaceborne Weather Radar Model and Geometry

Assuming a spaceborne radar carried by a satellite is located at a low altitude of 350 km. The radar's main beam scans in the cross-track direction, which is in the plane perpendicular to the moving direction of the satellite (along-track direction). Fig. 1 shows the radar scanning geometry. Compared to Hanado and Ihara (1992), which assumes an ideal pulse shape, Fig. 1(a) includes the shape of the "compressed pulse" where interference from neighboring gates is brought in by range sidelobes. Surface clutter area S is the area that antenna beam (both main beam and sidelobes) intercepts with the earth surface. S is determined by the main beam scanning angle Θ and radar pulse width, τ, and can be a ring or a circle depending on what portion of antenna pattern illuminates the surface. For comparison purpose, the radar is set to follow the parameters of the TRMM system (Kozu (2001), Kummerow (1998)), except that two kinds of waveform are incorporated. One is a rectangular pulse with 1.67 μs pulse width, the other waveform is a linear frequency modulated (LFM) pulse whose length is 20 μs and modulation bandwidth is 2 MHz. Detailed configuration of the radar is given in Table 1. For the rectangular pulse, range resolution is 250 m and for the compressed LFM pulse, range resolution is 75 m. Electronic scanning is assumed, which leads to a wider main beam for off-nadir angles. If main beam scanning angle is Θ , the beamwidth becomes $\theta_1/\cos(\Theta)$.

Height	**350 km**
Frequency	**13.8 GHz**
Scan angle	**17° with 0.71° step**
Transmit power *P_t*	**616 watts**
Antenna gain *G*	**47.4 dB**
Antenna main beam width	**0.71°**
Rectangular pulse width	**1.67 μs**

Rectangular pulse resolution	**250 m**
LFM pulse width, τ	**20 μs**
LFM bandwidth, β	**2 MHz**

Table 1. Spaceborne weather radar configuration

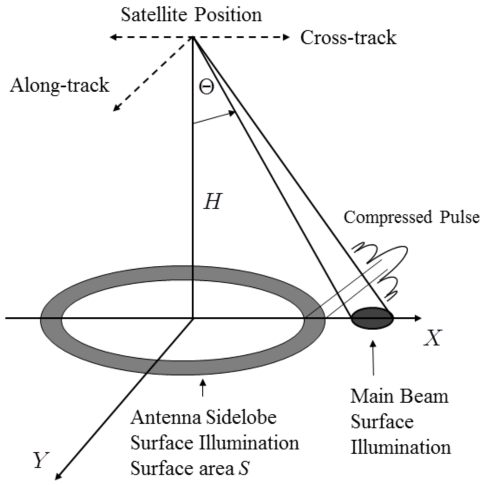

(a)

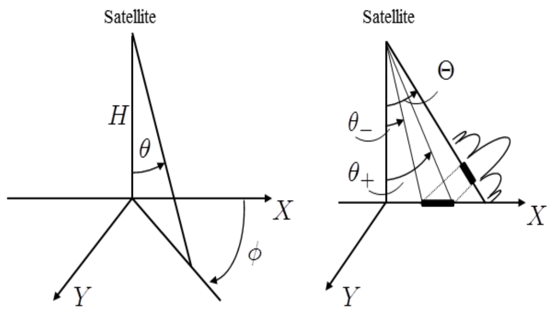

(b) (c)

Figure 1: (a) Typical spaceborne weather radar geometry (b) coordinate system, (c) geometrical view in "XH plane". $\theta_{\pm}$ is defined in and Eq. (11) (Hanado and Ihara (1992)).

3.2 Land and Sea Clutter Models

Modeling surface clutter returns is important for spaceborne radar as surface clutter interference through both antenna and pulse compression exists where distances of radar range gates are close to or greater than the height of the satellite. Thus, better prediction of backscattered power from ground and sea clutter would lead to more realistic simulations.

Radar cross section (RCS) of land and sea are usually characterized by the normalized RCS parameter σ_0 (in m^2/m^2) and varies as the incidence angle changes (θ in Fig. 1(a)). It is also different when the physical conditions of the surface change. For example, RCS of sea depends on the surface wind speed and RCS of land depends on the surface roughness. In this study, RCS of sea is expressed as a function of the incidence angle and parameters that describe the sea surface condition as described in Hanado and Ihara (1992), and Meneghini and Atlas (1986). For land surface, clutter model proposed by Morchin (1990) is adopted.

For sea surface,

$$\sigma_0(\theta) = \sigma_0(0) \cdot \sec^4\theta \cdot \exp\left(-\frac{-\tan^2\theta}{s^2}\right) \qquad (1)$$

where $\sigma^0(0)$ is the normalized RCS when the incident angle θ is $0°$ and s is the total variance of surface slopes given in Table 2.

Wind Condition	$\sigma^0(0)$	s
Weak (1 m/s)	15.99 dB	0.1397
Moderate (7.5-10 m/s)	11.51 dB	0.1959
Strong (64 m/s)	7.391 dB	0.3515

Table 2: Sea surface model parameters in different wind condition

Fig. 2(a) (b) show the normalized RCS of land and sea for different incidence angles computed from these models. Details of the land surface model can be found in Morchin (1990), and Schleher (2009). Four different terrains including desert, farmland, wooded hills and mountains are incorporated.

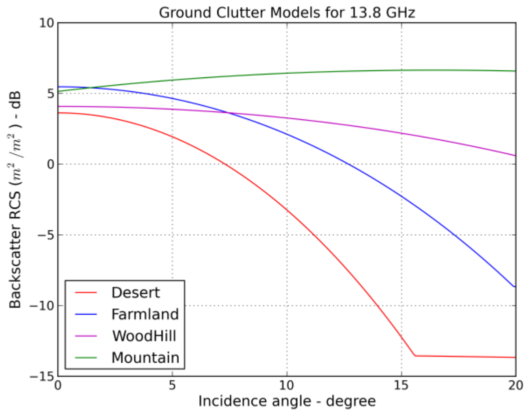

(a)

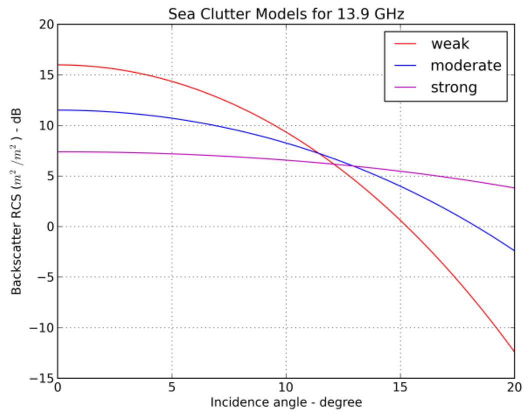

(b)

Figure 2: Normalized RCS versus Incidence Angle for Land (a) and Sea Clutter (b).

3.3 Antenna and Pulse Compression Receiver Models

In this study, the antenna pattern is modeled as a Gaussian shaped main beam with flat sidelobes. Though this model is simple, it provides the "worst case" performance benchmark for specific antenna patterns (with different mainbeam width and different sidelobe structures). In the log domain, the antenna pattern is expressed as

$$g(\theta') = \begin{cases} G_{SL} & \text{If } -12(\theta'/\theta_1)^2 < G_{SL} \\ -12(\theta'/\theta_1)^2 & \text{Otherwise} \end{cases} \quad (2)$$

where θ' is the elevation angle related to antenna boresight ($\theta' = 0$), G_{SL} is sidelobe level and θ_1 is the half power beam width. Fig. 3 shows an example of the simplified beam pattern with main beam width 0.71° and sidelobe level -35 dB. Here a circularly symmetric antenna pattern is assumed, otherwise it would be $g(\theta', \phi')$. Eq. (2) is not defined in the radar global coordinates illustrated in Fig. 1(b), transforming from the antenna pattern coordinates to the radar global coordinates is given in Eq. (3).

$$\theta' = \cos^{-1}[\cos(\theta)\cos(\Theta) + \sin(\theta)\sin(\Theta)\cos(\phi)] \quad (3)$$

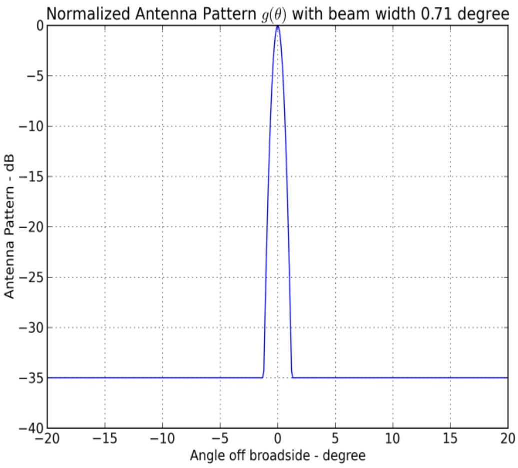

Figure 3: Normalized antenna pattern $g(\theta')$.

Pulse compression technique is widely used to achieve better range resolution. However, along with the nonlinearities in the sensor system, pulse compression introduces sidelobes that bring in the interference from neighboring resolution cells. In the spaceborne radar case, such interferences are severe as they are mainly from ground clutter returns, which are much stronger than weather returns. Similar to the antenna pattern model, range sidelobes effect from pulse compression is characterized by a simplified filter response as given in Fig. 3, where a - 40 dB sidelobe level is shown. The simplified filter response can be modified to accommodate different pulse compression waveforms and sidelobe suppression techniques. As pulse compression only affects range gates within a same range profile, the simulated return power after pulse compression yields

$$y(n) = \sum_{i=-(M-1)}^{M-1} s(i)x(n+i), \quad (4)$$

where $s(i)$ is the pulse compression receiver output, $x(n)$ is the return power for the n^{th} range gate in a range profile if a short pulse that has the same resolution is transmitted, and M is the rounded pulse compression gain (defined as $B\tau$), which determines the extent of range gates that are affected by the sidelobes. In this study, $M = 40$, $x(n)$ is essentially the "ground truth" or "impulse response" of scatterer response.

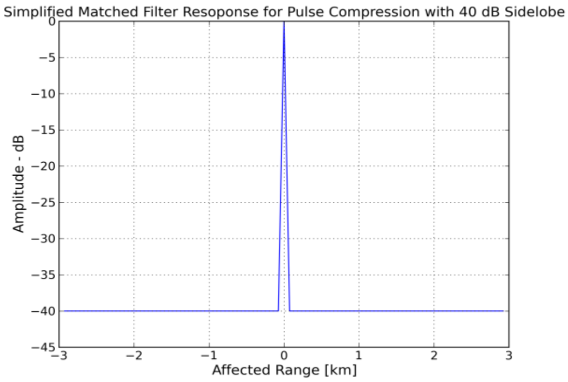

Figure 4: Simplified matched filter output for pulse compression with 40 dB sidelobe.

4. SIMULATION PROCEDURES

According to Doviak and Zrnic (2006), atmospheric return power can be calculated from the weather radar equation (no weather attenuation is included for the current simulation):

$$P_a = \frac{P_t G^2 \lambda^2}{(4\pi)^3 r^4 l^2} \cdot \frac{c\tau\pi\theta_1^2}{16\ln 2} \cdot \eta \quad (5)$$

Where P_t is the transmitted power, G is the antenna gain at boresight, θ_1 is the high power beam width, τ is pulse width, r is the range of the bin, and l is the one-way propagation loss due to clear-air attenuation. *Reflectivity* η describes the average RCS of hydrometeors per unit volume and is computed from

$$\eta = \frac{\pi^5}{\lambda^4}|K_w|^2 Z \quad (6)$$

Where K_w is the dielectric factor of water and Z is called the reflectivity factor and it is usually transferred from [mm^6 m^{-3}] to dBZ [10log (mm^6 m^{-3})] for a smaller dynamic range. According to Olsen (1978), for 13.8 GHz (Ku-band), reflectivity factor Z and rainfall rate R is related by

$$Z = 245R^{1.33} \quad (7)$$

which is illustrated in Fig. 5.

In addition to the signal returns from antenna main beam, interference echoes at the same range from antenna sidelobes are received by the radar simultaneously. At range smaller than the height of the satellite, interference is mainly from atmospheric targets and can be neglected unless a large gradient of reflectivity exists. However, at range gates larger than the height of the satellite, antenna mainlobe/sidelobes intercepts the ground and interference of surface clutter cannot be neglected since surface clutter returns are much stronger than atmospheric returns.

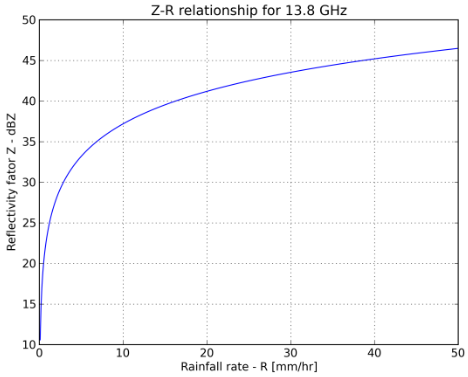

Figure 5: Z-R relationship for 13.8 GHz (Ku-band).

As shown in Hanada and Ihara (1992), and Tagawa (2007), surface clutter returns through both antenna mainbeam and sidelobe can be computed by integrating the following radar equation over the surface area S in Figure 1(a):

$$P_s = \frac{P_t G^2 \lambda^2}{(4\pi)^3} \int\int_S \frac{g^2 \sigma_0 l^2}{r^4} \mathrm{d}S \quad (8)$$

Depending on the main beam scanning angle, radar pulse width and range for the radar bin, the surface area of integration is a circle for $2H/c < t < 2H/c + \tau$ and an annulus for $t > 2H/c + \tau$ with flat-earth approximation. *t*=0 is correspondent to the leading edge of a pulse sent from the transmitter. Incorporated with the simplified antenna pattern used in this study, Eq. (8) can be further written as

$$P_s = \frac{P_t G^2 \lambda^2}{(4\pi)^3} \cdot \frac{1}{H^2} \int_{\theta_-}^{\theta_+} F^2(\theta)\sigma_0(\theta) l^2 \mathrm{sin}2\theta \mathrm{d}\theta \quad 9)$$

Where $\sigma_0(\theta)$ is the normalized RCS given in Eq.(1). The integral interval $[\theta_-, \theta_+]$ (shown in Fig. 1(b)) can be calculated from

$$r_\pm = r \pm c\tau/4 \quad (10)$$

$$\theta_\pm = cos^{-1}(H/r_\pm) \quad (11)$$

$F(\theta)$ in Eq. (9) is defined as the normalized ϕ-integrated squared antenna pattern and yields

$$F(\theta) = \int_{-\pi}^{+\pi} g(\theta, \phi)\mathrm{d}\phi \quad (12)$$

where $g(\theta, \phi)$ is the normalized antenna pattern in global coordinate system and it can be computed from Eq. (2) and (3). Fig. 4 shows $F(\theta)$ for beam scanning angle $\Theta = 4°$, $\Theta = 8°$ and $\Theta = 12°$. As it is shown, $F(\theta)$ has a fixed sidelobe level at about -55 dB for this case and the main beam gain decreases as the radar scans farther away from nadir direction. Note that for Eq. (10) and (11), if θ_+ is imaginary for a range bin, there is no interference from surface clutter for that range bin as it doesn't reach the ground ($S = 0$); if θ_+ is real but θ_- is imaginary, the surface area S is a circle and θ_- is set to 0 for the integration in Eq. (9); if both θ_+ and θ_- are real, the surface area S is a ring.

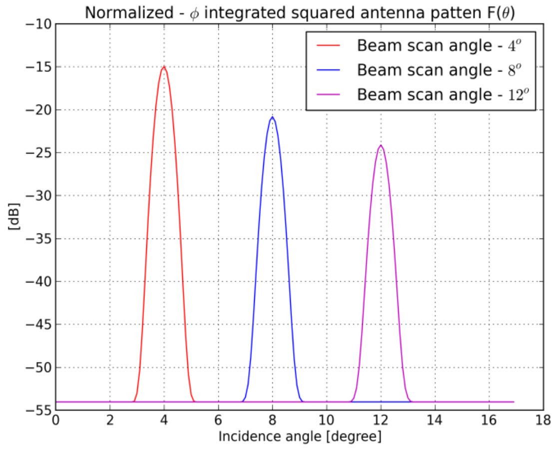

Figure 4: normalized ϕ-integrated squared antenna pattern $F(\theta)$ for three different beam scanning angles.

For every range resolution cell, power returns from atmosphere (P_a) and surface clutter (P_s) are computed from Eq. (5) and (8) if any atmosphere or surface clutter exits. These two equations do not incorporate the pulse compression sidelobe interferences, therefore, the "range-sidelobe-free" return power for the n^{th} range gate in a range profile yields

$$x(n) = P_a(n) + P_s(n) \quad (13)$$

Pulse compression effects are then calculated according to Eq. (4).

From weather radar equation, it is possible to convert atmospheric return power (P_a) to reflectivity factor Z in dBZ by the following simple manipulation:

$$10\log[Z] = 10\log[P_a] + 20\log[l] + 20\log[r] + 10\log[C] \quad (14)$$

where C is called the *system calibration factor*. If a weather resolution cell with a particular reflectivity is artificially put in the simulated airspace and the simulator outputs P_a, system calibration factor C can be calculated from Eq. (14). In this simulation, a weather target of 50 dBZ leads to $C = 49.5$. Therefore, surface clutter returns P_s can also be converted to dBZ unit using

$$10\log[Z] = 10\log[P_s] + 20\log[l] + 20\log[r] + 10\log[49.5] \quad (15)$$

5. RESULTS AND DISCUSSION

5.1 Impacts of Surface Clutter Without Pulse Compression

Sea clutter returns for weak wind condition and strong wind condition are shown in Fig. 5(a) and (b). These results match very well with the published actual radar measurement data (Durden (2001) and Hanado and Ihara (1992)). In the two figures, the white area is the clutter free area where no interference from the surface exists. The dark blue area is the sidelobe clutter area. For weak wind, the average power level is about 20 dBZ and for strong wind, it is about 15 dBZ. From Eq. (7), rainfall rate 0.5 mm/hr corresponds to 20 dBZ. Thus in this sidelobe clutter area, signal to clutter ratio is above 0 dB. The red area is the main beam clutter area (surface area S is a circle), the power level is above 40 dBZ at an altitude of about 1.5 km and beam scanning angle 17^o . In this area, clutter interference is severe, any rainfall lower than 20 mm/hr will be completely masked by surface interference through antenna sidelobe. The reason for the "saw tooth" structure in the reflectivity map is due to the fact that the range resolution cells are not parallel to the ground as the beam scans off nadir direction. Such "saw tooth" structure may be less significant if a smaller beam scanning step is implemented.

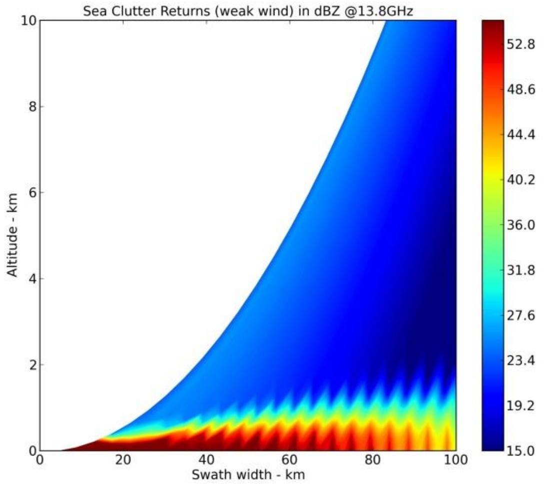

(a)

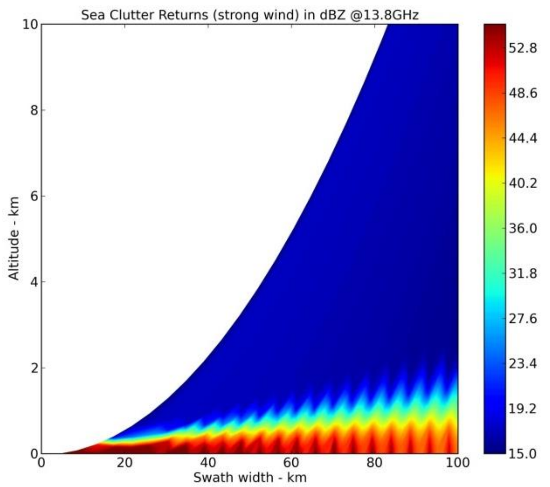

(b)

Figure 5: Sea clutter returns through antenna sidelobe for weak wind condition (a), and strong wind condition (b).

5.2 Impacts of Surface Clutter With Pulse Compression

Surface clutter returns through antenna and pulse compression sidelobe for sea surface with weak wind condition and desert surface are illustrated in Fig. 6(a), and (b). As it can be seen, clutter interference level greatly increases to about 3 km at nadir direction due to range sidelobes. The height of affected area is related to the LFM pulsewidth. For Pulse compression sidelobe level at - 40 dB, power level of the clutter interference is above 30 dBZ for basically anywhere lower than 1.5 km, which is a significant issue and no rainfall lower than 10 mm/hr will be measured precisely within that area.

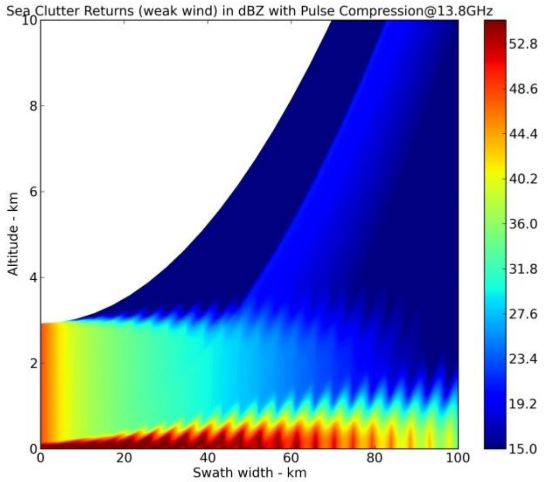

(a)

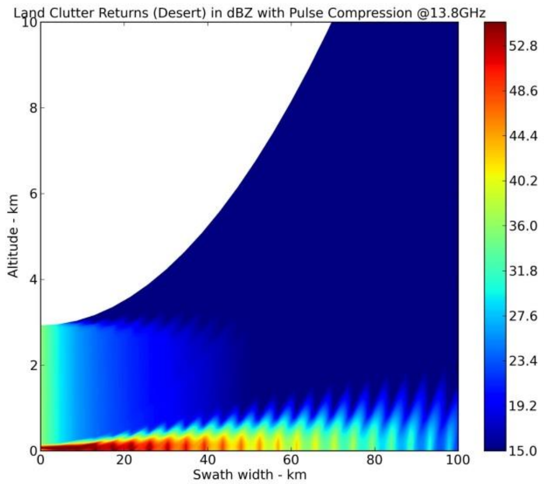

(b)

Figure 6: Surface clutter returns through antenna and pulse compression sidelobe for sea surface with weak wind condition (a) and desert surface (b). Pulse compression sidelobe level at 40 dB for both plots.

Fig. 7(a), and (b) show the same surface clutter returns through antenna and pulse compression sidelobe for sea surface with weak wind condition and desert surface as those in Fig. 6, except that pulse compression sidelobe level is at 60 dB in Fig .7. It is quite obvious that clutter power level is much lower than it is in Fig. 6. For pulse compression sidelobe level at 60 dB, signal to clutter ratio of the observation is about the same as that in Fig. 5 where surface clutter interference through antenna sidelobes dominates.

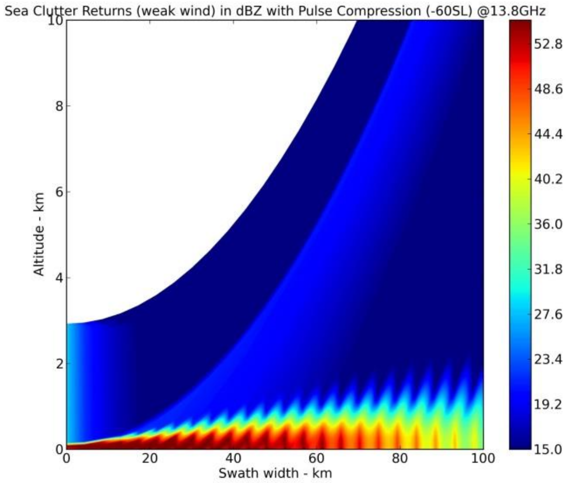

(a)

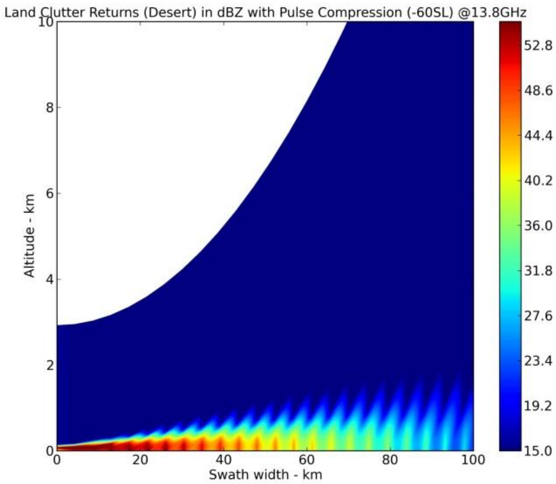

(b)

Figure 7: Surface clutter returns through antenna and pulse compression sidelobe for sea surface with weak wind condition (a) and desert surface (b). Pulse compression sidelobe level at 60 dB for both plots.

6. CONCLUSION

Surface clutter echoes through antenna sidelobes AND range sidelobes from pulse compression can severely interfere with the atmospheric returns near the earth surface for spaceborne weather radar. To help predict the performance of the designed spaceborne weather radar system in presence of surface clutter interference, a radar simulator is developed to quantify the power level of surface clutter returns in dBZ. Radar system parameters including antenna sidelobe level are mainly taken from the TRMM radar except that a LFM pulse is assumed in order to evaluate the range sidelobe effects from pulse compression. Two range sidelobe levels are studied. For 40 dB range sidelobe level, intense interference which is larger than 35 dBZ is observed basically anywhere lower than 1.5 km. For 60 dB range sidelobe level, interference from range sidelobes can be ignored as the power level of interference is close to the interference through only antenna sidelobes.

In future study, the spaceborne radar simulator will be further extended to include different system losses and power amplifier nonlinearities. Practical antenna pattern and pulse compression filter response will also be incorporated. Furthermore, the designed sensor system may need to observe weak atmospheric targets, such as light rain and clouds, as well as severe storms. Is the system capable of detecting weak signal from distance with strong attenuation? As a simulated weather field at fine scales over various atmospheric conditions has been made possible by advanced numerical weather models (Zhengzheng (2011)), incorporating both atmospheric and sensor system effects into the radar simulator is feasible and will be developed to address those questions.

7. ACKNOWLEDGMENT

This work is supported by NASA-EPSCoR grant NNAX11AM10A. The authors would like to express sincere appreciations to the researchers and engineers in NASA-GSFC.

8. REFERENCES

Doviak, R. J. and D. S. Zrnic. Doppler Radar and Weather Observations. 2nd. Dover Publications, 2006.

Durden, S.L., et al. "Surface clutter due to antenna sidelobes for spaceborne atmospheric radar." Geoscience and Remote Sensing, IEEE Transactions on 39.9 (2001): 1916-1921.

Hanado, H. and T. Ihara. "Evaluation of surface clutter for the design of the TRMM spaceborne radar." Geoscience and Remote Sensing, IEEE Transactions on 30.3 (1992): 444-453.

Kozu, T., et al. "Development of precipitation radar onboard the Tropical Rainfall Measuring Mission (TRMM) satellite." Geoscience and Remote Sensing, IEEE Transactions on 39.1 (2001): 102-116.

Kummerow, Christian, et al. "The Tropical Rainfall Measuring Mission (TRMM) Sensor Package." J. Atmos. Oceanic Technol. 15.3 (1998): 809-817.

Levizzani, Vincenzo, Peter Bauer and Joseph F. Turk. Measuring Precipitation from Space: EURAINSAT and the Future. Springer, 2007.

Li, Lihua, et al. "High-Altitude Imaging Wind and Rain Airborne Radar (HIWRAP)." Geoscience and Remote Sensing Symposium, 2008. IGARSS 2008. IEEE International. 2008. III - 354-III - 357.

Li, Zhengzheng, et al. "A Microphysics-Based Simulator for Advanced Airborne Weather Radar Development." Geoscience and Remote Sensing, IEEE Transactions on 49.4 (2011): 1356-1373

Meneghini, Robert and David Atlas. "Simultaneous Ocean Cross Section and Rainfall Measurements from Space with a Nadir-Looking Radar." J. Atmos. Oceanic Technol. 3.3 (1986): 400-413.

Morchin, W. C. Airborne Early Waring Radar. Artech House, 1990.

Olsen, R., D.V. Rogers and Daniel B. Hodge. "The aRb relation in the calculation of rain attenuation." Antennas and Propagation, IEEE Transactions on 26.2 (1978): 318-329.

Pavone, S, et al. "Measurement simulations from spaceborne weather radar." Physics and Chemistry of the Earth, Part B: Hydrology, Oceans and Atmosphere 25 (2000): 883-888.

Schleher, D. C. MTI and Pulsed Doppler Radar with Matlab. Artech House, 2009.

Tagawa, T., et al. "Suppression of Surface Clutter Interference With Precipitation Measurements by Spaceborne Precipitation Radar." Geoscience and Remote Sensing, IEEE Transactions on 45.5 (2007): 1324-1331.